The detection and dimension of bubble entrainment and comminution

T. G. Leighton,[a] P. R. White, and M. F. Schneider

Institute of Sound and Vibration Research, University of Southampton, Highfield, Southampton SO17 1BJ, United Kingdom

Data on bubble entrainment and comminution are gathered in three experiments, involving the breakup of a disk of air trapped between two plates, and bubble cloud generation under a waterfall, and a plunging jet. In the second two cases, an automated acoustic system for characterizing the entrainment is employed. The data sets are compared with an existing theory for bubble fragmentation, in which a key parameter is the number of spatial dimensions associated with the insertion of randomly positioned planes which are used to divide up the bubble. While an appropriate best-fit theoretical curve can be obtained for the bubble population histograms generated by air disk comminution, waterfalls and plunging jets produce multimodal distributions which the theory cannot model. The differing roles of shape oscillations and surface waves in bubble fragmentation, and the issues involved with incorporating these into the model, are examined. © *1998 Acoustical Society of America.* [S0001-4966(98)04804-8]

PACS numbers: 43.30.Gv, 43.25.Yw [DB]

INTRODUCTION

Bubbles may be generated through a number of common processes, all of which relate to changes (formation, rupture, closure, merging, etc.) of one or more gas/liquid interfaces. Bubbles may, for example, be entrained from an approximately planar free surface; or a population might be generated through comminution of an existing gas pocket. Energy from such processes, channeled through mechanisms involving surface tension, hydrostatic, and hydrodynamic forces, etc., can generate bubble oscillation and consequently acoustic emission. Minnaert[1] predicted that the natural frequency should vary inversely with bubble size. The bubble, behaving to first order as a lightly damped single degree of freedom oscillator,[2] emits on entrainment an acoustic "signature" resembling an exponentially decaying sinusoid.[3,4] Identification of these has enabled size distribution spectra from the acoustic emissions of bubbles entrained in brooks, streams, and waterfalls to be obtained.[5] The passive acoustic emissions associated with bubble formation, including such signatures, have been examined in a large number of scenarios. Examples include the formation of bubble clouds by injection[6] or by the impact of bodies of water.[7–10] Several studies have examined entrainment by liquid jets.[11–16] Acoustic emissions and "signatures" have been identified with other forms of liquid drop impact, including rainfall,[17–20] and wave breaking.[21,22] Such studies have in turn led to studies of the underlying fluid dynamics[23,24] and investigations of the possibility of using the acoustic signals for monitoring purposes.[25–29]

Longuet Higgins[30] produced an analysis which demonstrated how the problem of predicting the number and size of daughter bubbles might be approached and, noting the dearth of laboratory data, compared the theory with the measurements of earlier workers.[5,31–33]

The entrainment is modeled by the dissection of a cubical air body through the insertion of planes. The newly formed bubbles ("daughters") are represented by the rectangular sub-blocks thereby generated. Three sets of planes exist, each set being parallel to a face of the cube and containing m planes. The dimensionality (D) of the fragmentation reflects the number of sets used. The sets are inserted independently to one another (Fig. 1). For comparison of theory and experiment, the dimensionality and the number of planes are chosen to best fit the standard deviation and skewness of the data, and the height of the theoretical curve is adjusted to relate to the total number of bubbles and the bin width.

In the natural world Longuet Higgins suggested that a one-dimensional event may occur when water is running over a smooth stone and entrains a cylindrical volume of air. The one-dimensional model considers a line segment of unit length, which is divided by m points spaced randomly into $m+1$ subsegments of typical length X. The probability density $p(X)$ of the length of this subsegment is

$$p(X) = m(1-X)^{(m-1)}$$

$$\text{(provided } 0 < X < 1 \text{ and } m > 1), \tag{1}$$

and the cumulative probability function $P(X)$ is given by

$$P(X) = \int p(X) \, dX. \tag{2}$$

The derivative of the cumulative probability function $P(X)$ with respect to $\ln(X)$ gives the density of the distribution:

$$\frac{dP}{d\{\ln(X)\}} = \frac{dP}{dX} \frac{dX}{d\{\ln(X)\}} = p(X)X = m(1-X)^{(m-1)}X. \tag{3}$$

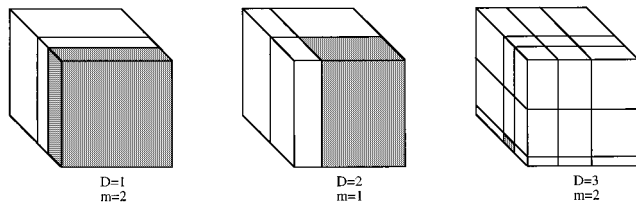[a]Electronic mail: tgl@isvr.soton.ac.uk

FIG. 1. The model of bubble fragmentation: a cube which is split by m planes inserted from D dimensions (each coordinate axis being perpendicular to the respective cube face). One of the daughter bubbles produced in each case is shaded. (a) $D=1$, $m=2$; (b) $D=2$, $m=1$; (c) $D=3$, $m=2$.

Replacing the line segment of unit length, divided by m points, by a block of unit volume, divided by m parallel planes, the probability density of the sub-blocks will be exactly the same as shown above.

Let R denote the radius of a spherical bubble of volume V, and R_0 the radius of a bubble of volume V_0, such that the normalized bubble radii and volume are $r=R/R_0$ and $\nu=V/V_0$, respectively. The density of the distribution of bubble radii is given by:

$$\frac{dP}{d\{\ln(r)\}} = \frac{dP}{dV}\frac{dV}{d\{\ln(r)\}}$$
$$= p(v)3v = m(1-v)^{(m-1)}3v. \quad (4)$$

In the two-dimensional model a cubical block of unit volume, which is split by two sets of perpendicular and independent planes, is considered. The distributions are calculated using numerical integration. In a similar way the model can be extended to three dimensions, with distributions having a much smaller mean. In all three cases the distributions for a large number of planes tend to limiting values of nonzero standard deviation and skewness.

In this paper visual observations of air disc fragmentation lead to studies of bubble entrainment in a waterfall and under a plunging jet in the laboratory. The comparison between the data sets and the theory is discussed in terms of the assumptions inherent in the model, and the relative effectiveness of visual and acoustic techniques for monitoring bubble entrainment.

I. OPTICAL METHODS

A so-called ''two-dimensional'' bubble (an ''air disk'') was formed by injecting an air bubble into degassed water between two plates of polymethylmethacrylate (PMMA) separated by an O-ring. The energy for fragmentation is provided by a repeatable combination of flow and pressure disturbance. The apparatus consists of a U-tube which is partially filled with degased water. It is connected by a hose to the PMMA plates at one end, and is stoppered at the other by a top plate which can be opened (Fig. 2). The bubble, which is initially positioned at the center of the plates using a magnetic slider, expands when the vacuum pump reduces the ambient pressure. The top plate is then rapidly opened, and the resulting liquid pressure change causes bubble oscillation, which is video recorded at 50 f.p.s. (frames per second), 1-ms exposure. The minimum pressure applied to the bubble was 20 mbar (approximately 10 mbar higher than the vapor
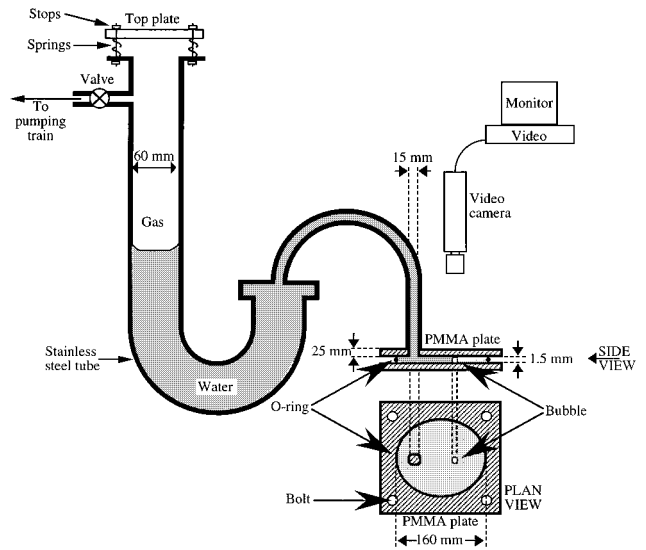

FIG. 2. The apparatus employed to fragment air disks, showing the U-tube equipment; and both plan and side views of the PMMA plates.

pressure of water at 20 °C). The pre-expansion and pre-collapse size of the bubble and its daughters were measured using a graticule magnifying glass. The partial vacuum caused deflection of the plates of about 0.2 mm in the center and 0.06 mm at the O-ring when the lowest pressure was applied. This deflection was taken into account when the bubble volumes were calculated. The release of the pressure leads to an oscillation of the plates (measured by accelerometer to be at 30 Hz and of 0.5-s duration) and an oscillating water flux. Bubbles having radii smaller than the distance between the plates were hemispherical, rather than cylindrical (Fig. 2). Since the third dimension may influence the dynamics of such bubbles significantly more than for the larger air disks, the transitional size between the two is indicated on the plots of the results (Fig. 6). In general 10–30 breakups of one bubble size at a particular pressure were recorded to obtain representative histograms of daughter bubbles. The accuracy of the measurement of the bubble volume was $\pm5\%$. (Reference 34 describes how the same apparatus can be modified to generate sonoluminescence from more energetic bubble collapses.)

II. ACOUSTIC MEASUREMENTS OF ENTRAINMENT THROUGH LIQUID IMPACT

A. Automated bubble signal recognition

Bubble generation was monitored through the use of the passive acoustic emissions. Hydrophone data from waterfalls and brooks had previously been examined,[5] and the time series found to contain distinct exponentially decaying sinusoids which are characteristic of bubble entrainment. These were used to obtain the size distribution of entrained bubbles from the frequencies of the sinusoids. However in noisy environments and with higher entrainment rates (where such ''signatures'' overlap), individual entrainments may not be detected with this technique. Nevertheless a time-frequency representation (TFR) via the Gabor coefficients (see the Appendix) can readily identify the bubble signatures (e.g., from
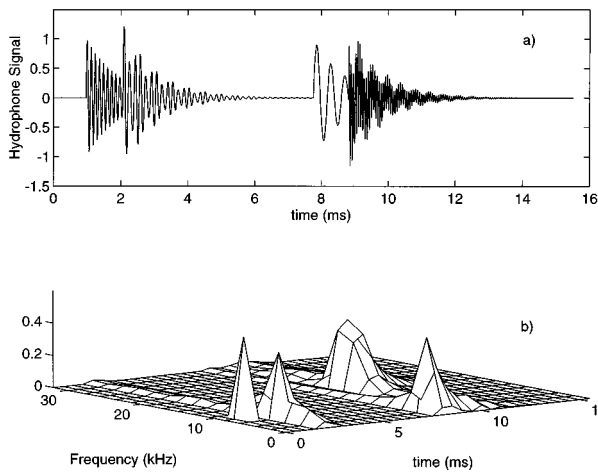
FIG. 3. (a) A noise-free test signal (artificial data) consisting of four exponentially decaying sinusoids. All have unit amplitude, with center frequencies 8, 6, 2.3, and 15.2 kHz, with epochs at 1, 2.12, 8, and 9.1 ms, respectively. All the signals have e-folding decay rates of 0.5 ms^{-1}. (b) Time-frequency representation of the magnitude of the Gabor coefficients associated with the time series of (a) (computed using an FFT size of 32 samples and an assumed decay rate matching that of the simulation). The first transient lies exactly on the sampling lattice of the Gabor expansion; the second lies on the lattice in frequency but not in time; the third lies on the lattice in time but not in frequency; and the fourth lies between lattice points in both frequency and time.
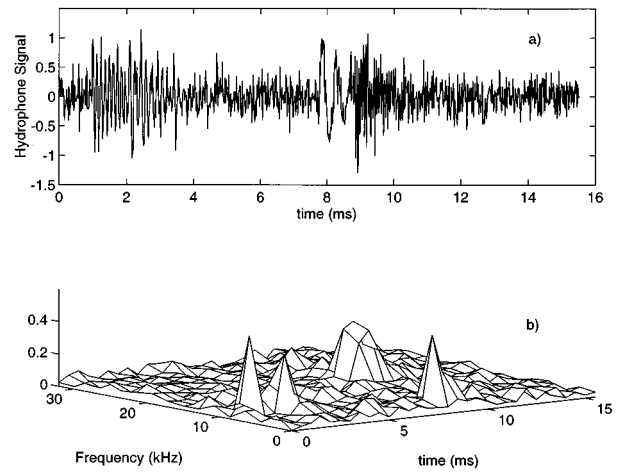
FIG. 4. (a) Same as for Fig. 3(a), but with the addition of Gaussian white noise, the standard deviation of which is 0.2. (b) Time-frequency representation of the magnitude of the Gabor coefficients associated with the time series of (a) (computed using an FFT size of 32 samples and an assumed decay rate matching that of the simulation).

rainfall over the ocean[35]). Resolution in time and frequency is a compromise determined by the size of the window imposed upon the data. The procedure employs a routine which thresholds on the value and gradient of the Gabor coefficients, then automatically counts and sizes the bubbles. For the calculation of the Gabor coefficients, a damping parameter with an e-folding time of 100 s^{-1} was assumed, and for bubble counting the threshold of the Gabor coefficient was set to be three times the mean value of the coefficients, with the gradient set equal to 0.3. These values were robust with respect to bubble counting. Entrainment data were gathered for analysis in this way in a small waterfall, and beneath a water jet which impacts a water surface from above.

Figures 3 and 4 show the efficacy of this technique on artificial data. Figure 3(a) depicts a noise-free test signal consisting of four transient components, each one being an exponentially decaying sinusoid, such that two overlapping pairs occur. In this example all these four components were chosen to have unit amplitude, with center frequencies 8, 6, 2.3, and 15.2 kHz, with epochs at 1, 2.12, 8, and 9.1 ms, respectively. All the signals had decay rates of 0.5 ms^{-1}. The Gabor coefficients are computed using an FFT size of 32 samples and an assumed decay rate matching that of the simulation. This time series was designed so that the first component lay exactly on the sampling lattice of the Gabor expansion, so that it could be represented by a single nonzero coefficient. The second component occurs at a frequency which is on the sampling lattice of the Gabor expansion, but occurs at a time which is between lattice points. The converse is true of the third component (which lies between lattice points in frequency, but on the sampling lattice in time). Finally the fourth component lies at a point which is on neither the time or frequency lattice. The effect of this

choice on the Gabor expansion can be seen in Fig. 3(b), which plots the magnitude of the Gabor coefficients as a function of time and frequency. The first component generates a single-point spike. The second signal has a well defined peak in time but is smeared in frequency, whilst for the third the converse is true. The peak corresponding to the fourth component is smeared in both frequency and time. This inconsistency can be mitigated by computing the Gabor expansion at a greater number of points.[36] However, for computational ease, attention here is restricted to the critically sampled distribution,[37] which is adequate for the purposes of this investigation.

Figure 4(a) shows the same signal as Fig. 3(a) but with the addition of Gaussian white noise, the standard deviation of which is 0.2. In the Gabor expansion shown in Fig. 4(b) the peaks are still clearly evident whereas in the time series, Fig. 4(a), identification of signals typical of bubble entrainment is less easy.

B. Entrainment in a waterfall

The acoustic signals of newly entrained bubbles were measured in a brook on the Southampton University Campus on 25.05.93. The hydrophone (Brüel & Kjaer 8104), was mounted on a steel rod at 15 cm depth beneath mean water level in a bubble field created at the base of a small waterfall (height approximately 20 cm, called location A); and at 10 cm depth in a different bubble field approximately 30 cm away (location B). The water was running very smoothly over the step. Two sets of data were obtained at each location. The hydrophone output was amplified (Brüel & Kjaer 2635) and recorded (AIWA HHB 1 PRO DAT recorder, with flat frequency response from 20 Hz to 22 kHz) for 10 min at both locations. Subsequently, the data from the field recordings were transmitted through a low-pass filter (Barr and Stroud EF5/20, roll off approx. 48 dB/oct) into a data acquisition box, where they were acquired and digitized using the MATLAB software package. The time history of the data
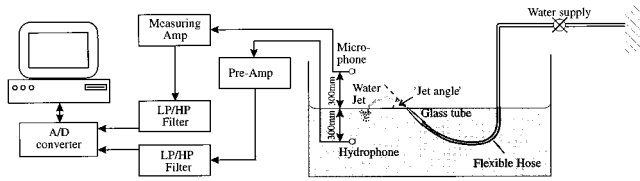
FIG. 5. Apparatus for entrainment by liquid jet.

showed that the most bubbles occurred in the frequency range between 500 Hz and 2 kHz. The signal was acquired with a sampling rate of 20 kHz while the low-pass filter was set to 10 kHz (although this provides no guard band to avoid aliasing, no significant frequency components were present above this frequency).

C. Entrainment by a plunging liquid jet

The experiment was carried out in a 1.8 m $\times$ 1.2 m $\times$ 1.2 m deep glass reinforced plastic tank which was filled to 1 m depth with fresh water. The tank was vibration isolated from the floor by Tico pads. A hose, terminating in a glass tube (5 mm inner diameter), was mounted near the water surface at varying angles (Fig. 5). Flow rate and jet angle were varied and recorded (the intention being to investigate the relative effect of these rather than characterize the jet completely[13–15]). The hydrophone (Brüel & Kjaer 8105) was at $\sim$300 mm depth beneath the entrained bubbles, but $\sim$150 mm off-axis. The hydrophone signal was amplified (Brüel & Kjaer 2635) and recorded on a DAT-recorder (AIWA, Type HOB 1 PRO) or fed directly through a low-pass filter (Barr & Stroud EF5/20) into the MATLAB data acquisition toolbox. The sample rate was 44 kHz, and the low-pass filter set with a cutoff frequency of 20 kHz.

III. OPTICAL RESULTS OF AIR DISC FRAGMENTATION

Figure 6 shows the daughter populations produced when a two-dimensional bubble having initial diameter d_0 = 7.5 mm expands under various pressure reductions to varying values of d_g, the diameter when fully expanded. The applied pressure reduction, and consequently the subsequent pressure step, were increased from the value just required to cause fragmentation. When a small pressure difference between applied pressure and atmospheric pressure was released, giving low excitation energy, two daughter bubbles were produced. With higher excitation energies, more daughters were created. In regard to the dependence on the initial bubble size, the release of a given pressure difference tended to produce an increased number of daughter bubbles, as d_0 increased.

The data in Fig. 6 are compared with the theory. The measured radii of the air discs were converted into radii of spheres R_{sph} with the same volume. Depending on the average number N_{avg} of daughter bubbles per break-up, the best value of m with the appropriate curve was fitted. In all the cases the data is fitted optimally when the one-dimensional theory for fragmentation is applied (D = 1). In Fig. 6(a) the average number of daughter bubbles is N_{avg} = 2. The best fit
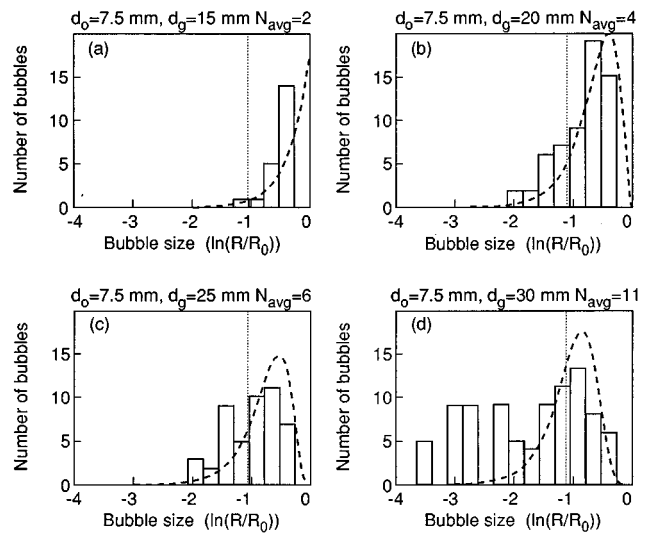

FIG. 6. Histograms of the distribution of daughter bubbles after fragmentation of an air disk of initial diameter d_0 = 7.5 mm for different excitation energies, with the best-fit curve from theory. The dotted vertical line shows the transition diameter, such that measured radii smaller than this are less than the plate spacing.

is given by the one-dimensional theory with D = 1 and m = 1, shown as the dashed line in Fig. 6(a). The theoretical curve does not fit the measured data, because no very large daughter bubbles were observed. This suggests that the preferred splitting occurred toward the middle of the bubble. This would give a more narrow distribution than would the random splitting that theory assumes. In Fig. 6(b) the excitation energy was increased, leading to an increased number of daughter bubbles. The mode of the measured bubble size distribution occurs at a smaller radius than does that of the prediction. A theoretical distribution having D = 1, m = 3, and N_{avg} = 4 [shown as the dashed line in Fig. 6(b)] gives the best fit. Figure 6(c) shows a similar distribution, but with a smaller mean and less sharp peak. Augmenting the applied pressure difference has generated an increased number of daughter bubbles. Again, the theoretical curve for a splitting in one dimension (D = 1), with an increased number of planes (m = 5, N_{avg} = 6), produces a better fit than is possible with the two- or three-dimensional theories. This optimal fit is shown by the dashed line in Fig. 6(c). Increasing the excitation energy still further leads to a greater number of daughter bubbles, as shown in Fig. 6(d). Most of the bubbles are smaller than the transitional size between disklike and hemispherical daughters, shown by the dotted vertical line. It is therefore not surprising that no single theoretical curve fits the entire data set in Fig. 6(d), since the processes involved in the fragmentation of hemispherical and disklike bubbles would be expected to differ. The figure shows the theoretical curve for D = 1, m = 10 tends to cover the disklike bubbles in the distribution.

The D = 1 best fit to the results suggests that the bubbles fragmented in a process where splitting occurred in one direction only. In addition, if the plane were inserted near the center of the bubble, this would give the more narrow distribution which is observed. These hypotheses are confirmed using high speed video pictures taken from the fragmentation
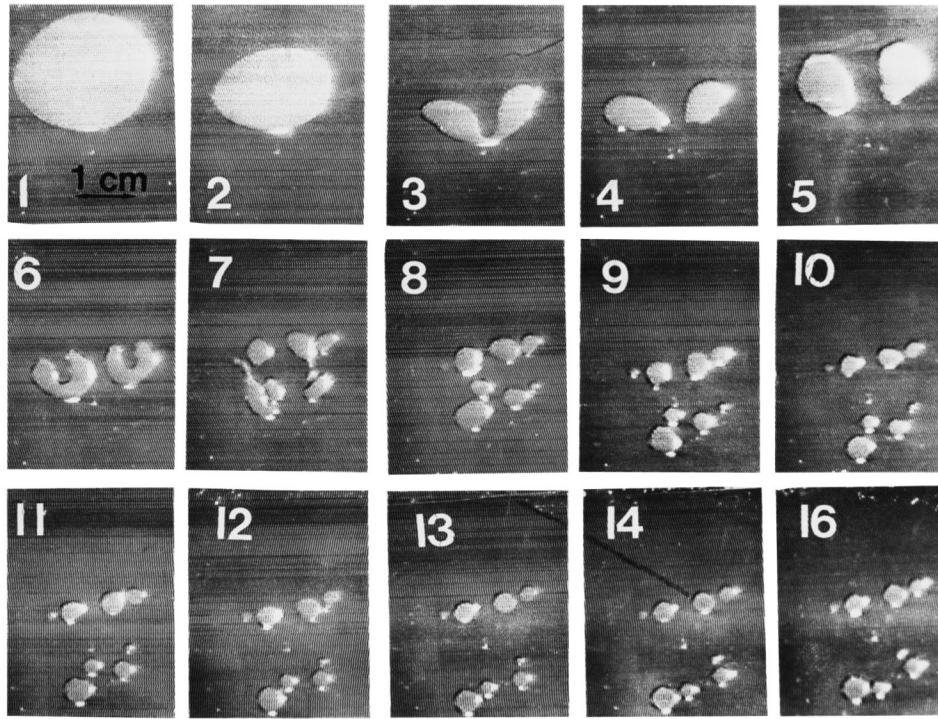
FIG. 7. Successive video images of air disc fragmentation (20-ms interframe time; $d_0 = 7.5$ mm; $d_g = 20$ mm). Between frames 1 and 2 the pressure is released, causing the bubble to lose its initially approximately circular profile.

of bubbles having pre-expansion diameters of $d_0 = 7.5$ mm (for pre-collapse diameters d_g of 20 and 25 mm). In Fig. 7, when the pressure is released the upstream wall involutes and forms a jet which travels across the cavity to impact the downstream wall (frame 3). This leads to the splitting of the bubble (frame 4), forming two daughter bubbles of approximately equal size (frame 5). These smaller bubbles undergo severe distortion from the circular shape and move with the water flux in the direction of the connector. This can be seen by comparing frame 4 and frame 6. It was found that with smaller excitation pressures (for example when $d_0 = 7.5$ mm and $d_g = 15$ mm), the process of bubble fragmentation stopped at this point, such that two ''daughters'' were formed from a single ''mother'' bubble. However with the stronger excitation used for Fig. 7 ($d_0 = 7.5$ mm and $d_g = 20$ mm), further fragmentation occurs. The daughter bubbles formed in frame 4 develop jets in turn, and are further split into smaller bubbles (frame 7). They are influenced by the movement of the plates and the associated water flux, and by the rebound of the pressure wave. The bubbles move as a result of the flux of the water around them (frames 8 and 9) and change their location and their shape for as long as 500 ms (this interval is the same as the time for which the PMMA plates oscillate). All of the daughter bubbles present at the end of the experiment were formed between frame 6 and frame 9. A variety of fragmentation behaviors was seen in other collapses, including the simultaneous formation of two jets (which are parallel in Fig. 8; and perpendicular in Fig. 9). Though the bubbles are subjected to similar excitations in Figs. 7 and 9, the collapses differ, primarily because of slight differences in the initial bubble shape.

IV. ACOUSTIC RESULTS FROM LIQUID IMPACT

A. In brook waterfall

The daughter bubble size distributions obtained at site A are shown in Fig. 10(a), and at site B in Fig. 10(b). Two data sets, (i) and (ii), were acquired at each site, showing that the general form of the histogram at each site was stable. Both sites exhibit two distinct peaks, the first at 400 Hz and the second at 1.2 kHz. At site A [Fig. 10(a)] the hydrophone was near to a bubble field having a frequency distribution from 700 to 1300 Hz, whereas at site B [Fig. 10(b)] the hydrophone record was dominated by the component at around 400 Hz. Visual observation indicated far too few bubbles large enough to account for the generation of this peak from individual entrainment signatures. Additionally, the time series showed that the signatures corresponding to the 400-Hz component were low amplitude and ill-defined, compared to the decaying sinusoids characteristic of the entrainment of smaller bubbles. These two facts suggest that this low-frequency peak arose through collective bubble oscillations,[38,39] and as such it was removed from the data set before comparison with theory. This comparison is shown in Fig. 11 for the same respective sites and times, where $dN/d[\ln(R_0)]$ is plotted as a function of R_0 (in keeping with the analysis of the Introduction with R_0 normalized to 1 mm throughout). The best fit to data is for a one-dimensional event ($D = 1$, $m = \infty$), as illustrated by comparison (through standard deviation and skewness) of the data with models of varying dimensionality and plane number (Fig. 12).

The theoretical curves in Fig. 11 are not so peaked as the experimental data, and show greater standard deviation. Comparing the time history with theory shows that the
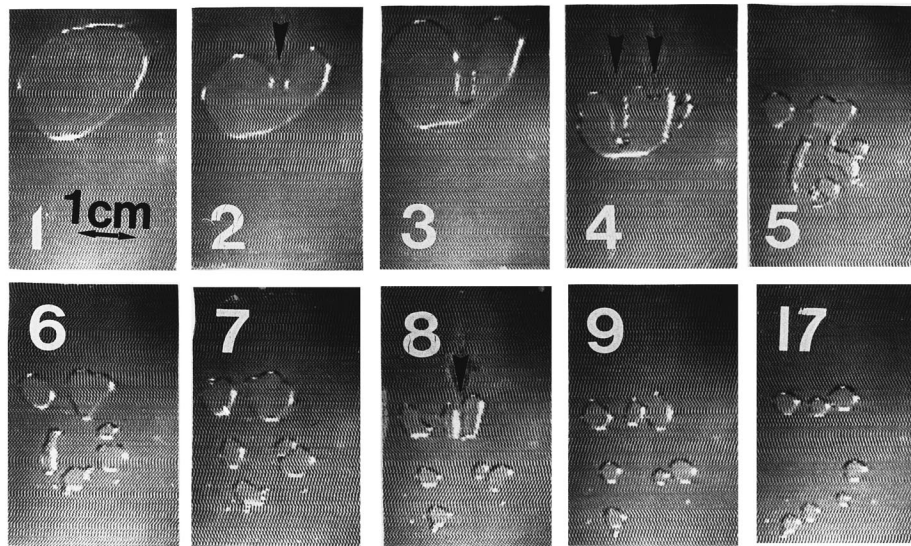
FIG. 8. Successive video images of air disk fragmentation (20-ms interframe time; $d_0 = 7.5$ mm; $d_g = 25$ mm). Between frames 1 and 2 the pressure is released. Two parallel jets (arrowed in frame 4) fragment the bubble (one jet appears before the other, as arrowed in frame 2). In frame 8 another jet, which causes a daughter bubble to fragment, is arrowed.

bubbles are entrained sequentially, rather than simultaneously, so that the data must be considered as summed distributions if comparison with theory is judging like against like.

B. Entrainment by plunging liquid jet

Investigation was made of the bubble size distribution entrained when a water jet strikes the surface of the water. The flow rate and the jet angle (measured between the horizontal and the direction of the water as it leaves the tube) were varied. Visual observation revealed that a minimum jet speed was needed to entrain bubbles, below which no entrainment occurred. The sole exception to this occurred when small surface waves on the water tank disturbed the water jet, resulting in bubble entrainment. Such surface waves

could be excited by entrained bubbles which rose to the surface by buoyancy. The maximum jet speed employed was limited to ensure that no subsequent splashes occurred. During the experiment it became clear that, for large angles, the main reason for entrainment was the disturbance of the water surface by bubbles rising to the surface. For smaller angles the water jet carried the entrained bubbles away from the jet and the waves on the tank surface set up when the bubbles burst did not affect the water jet.

Figures 13–15 show histograms of the bubble entrainment distributions. In part (i) of each figure the bubble count (N) is shown as a function of the bubble natural frequency. In part (ii), $dN/d[\ln(R_0)]$ is plotted as a function of R_0 to compare with the theory of the Introduction. Figure 13 shows results from an experiment with a constant water flow
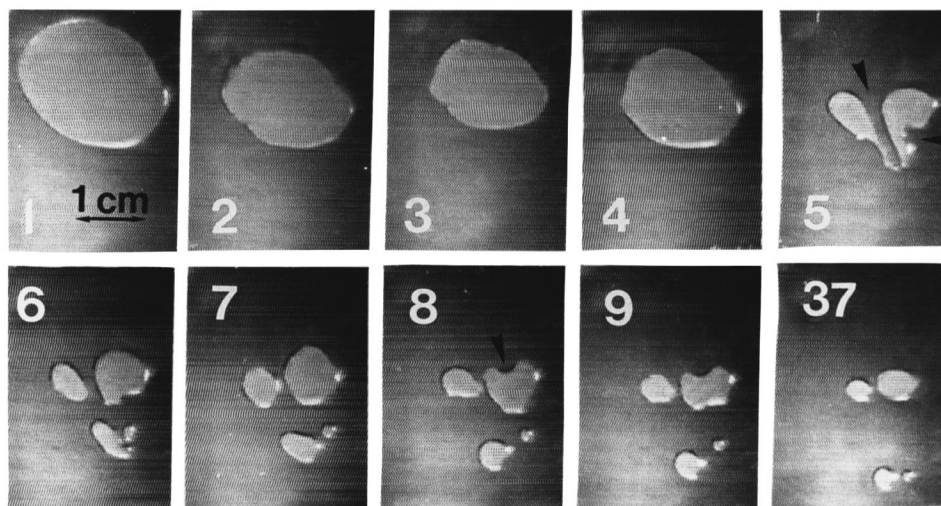

FIG. 9. Successive video images of air disk fragmentation (20-ms interframe time; $d_0 = 7.5$ mm; $d_g = 20$ mm). Between frames 1 and 2 the pressure is released. Two perpendicular jets fragment the bubble (arrowed in frame 5). In frame 8 the involution of a daughter bubble occurs (arrowed), but this is not sufficiently energetic to fragment the bubble.
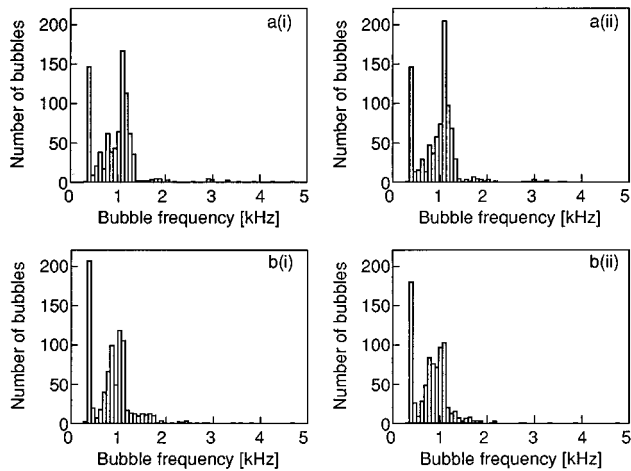
FIG. 10. Bubble resonance distributions (50 s of brook data each): (a): location A; (b) location B. Two data sets, (i) and (ii), are taken at each site. Acquisition: 10 ksamples/s with 5-kHz low-pass filter; damping 100 [s^{-1}]; Gabor coefficient for bubble count: threshold=3×mean, gradient=0.3. The number of samples in each data set was 500 000; with 128 sample points in each time interval for the TFR.

FIG. 12. The data from the waterfalls which were displayed in Fig. 11 are condensed to four points (°) on the standard deviation/skewness plane. The points are labeled (a)–(d) to show the dataset in Fig. 11 to which they refer. This display allows a comparison with the predictions obtained from various (D,m) combinations: For each of $D=1$, 2, and 3, the range of values from $m=1$ to $m=\infty$ is shown.

(2.5 l/min) and jet angles of 80°–30°. As expected from the visual observations outlined above, the number of bubbles entrained per time interval first decreased with a decreasing angle and then increased again. All the distributions showed a maximum at ~2 kHz. In addition they had a peak at ~700 Hz. At 80° the distribution is roughly monomodal, and the best fit to theory is one dimensional, both indicating a simple entrainment process. As the angle reduces to 60° the multimodal distribution is measured. Although the ''best'' fit is for $D=3$, the fit is poor, and suggests that processes not incorporated in the theory (such as coalescence, and the simultaneous occurrence of several types of entrainment and comminution) are involved. The entrainment rate decreases sharply (75°) and then gradually increases again. High frequencies are generated. The rate remains high from 55° to 30°, for which $D=2$ is the best fit, and which have distributions that are less multimodal, but still not as simple as for 80°.
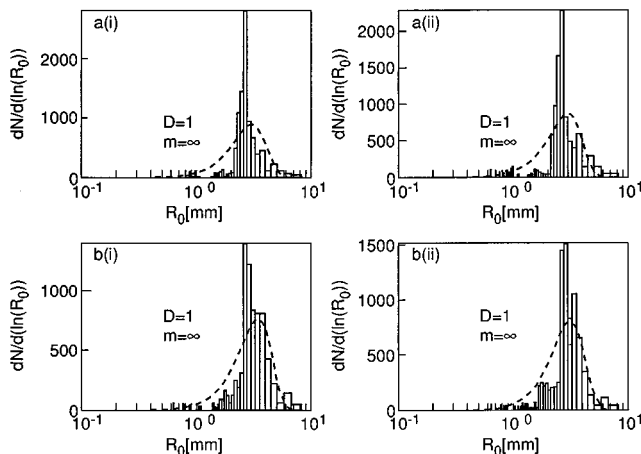

FIG. 11. Comparison of measured bubble density distributions with theoretical curves for $D=1$ and $m=\infty$ are shown. R_0 is normalized to 1 mm.
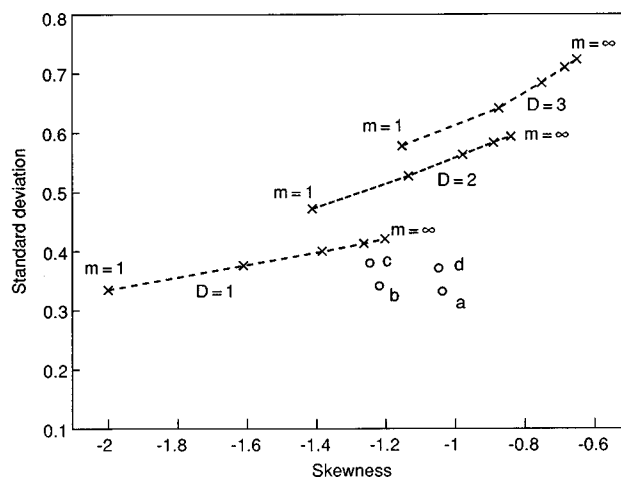
Figures 14 and 16 record the results for varying flow rates, and constant angles (55° in Fig. 14; 70° in Fig. 15). As expected, the numbers of bubbles entrained increases with flow rate in both cases. Multiple peaks are observed [see for example Figs. 14(b) and 15(b)]. Except for the trivially simple distribution presented in Fig. 15(a), the distributions are of the higher dimensions [$D=2$ or 3 throughout Fig. 14; $D=3$ for Fig. 15(b) and (c)].

V. DISCUSSION

This study reports measurements of three experimental systems: the comminution of a disk of air trapped between two solid plates; and the generation of bubble populations beneath a natural waterfall and a plunging liquid jet. The data sets are then compared with a theory which the author[30] sets out as being a simple, ''rough,'' first approach to the problem. As such, close agreement between theory and model would not be expected.

The best agreement is obtained for the most ''artificial'' scenario (in terms of geometry and mode of fragmentation), that is, the comminution of an air disk. In this, a single cavity breaks up, in keeping with a key assumption of the theory. The fit between theory and data is poorer for the two acoustically measured processes. Although attempts to find a best fit lead to the application of a one-dimensional model for the waterfall, and higher dimensions for the jet, even so the agreement is not good, with the occurrence of multiple peaks in the measured distributions (the current theory can only produce unimodal fits).

There are a number of factors which, while being intrinsic components of generation of bubble populations under waterfalls and plunging jets, do not have immediate counterparts in the theory. Both of these processes involve, to a greater or lesser extent, a surface. To a first approximation,
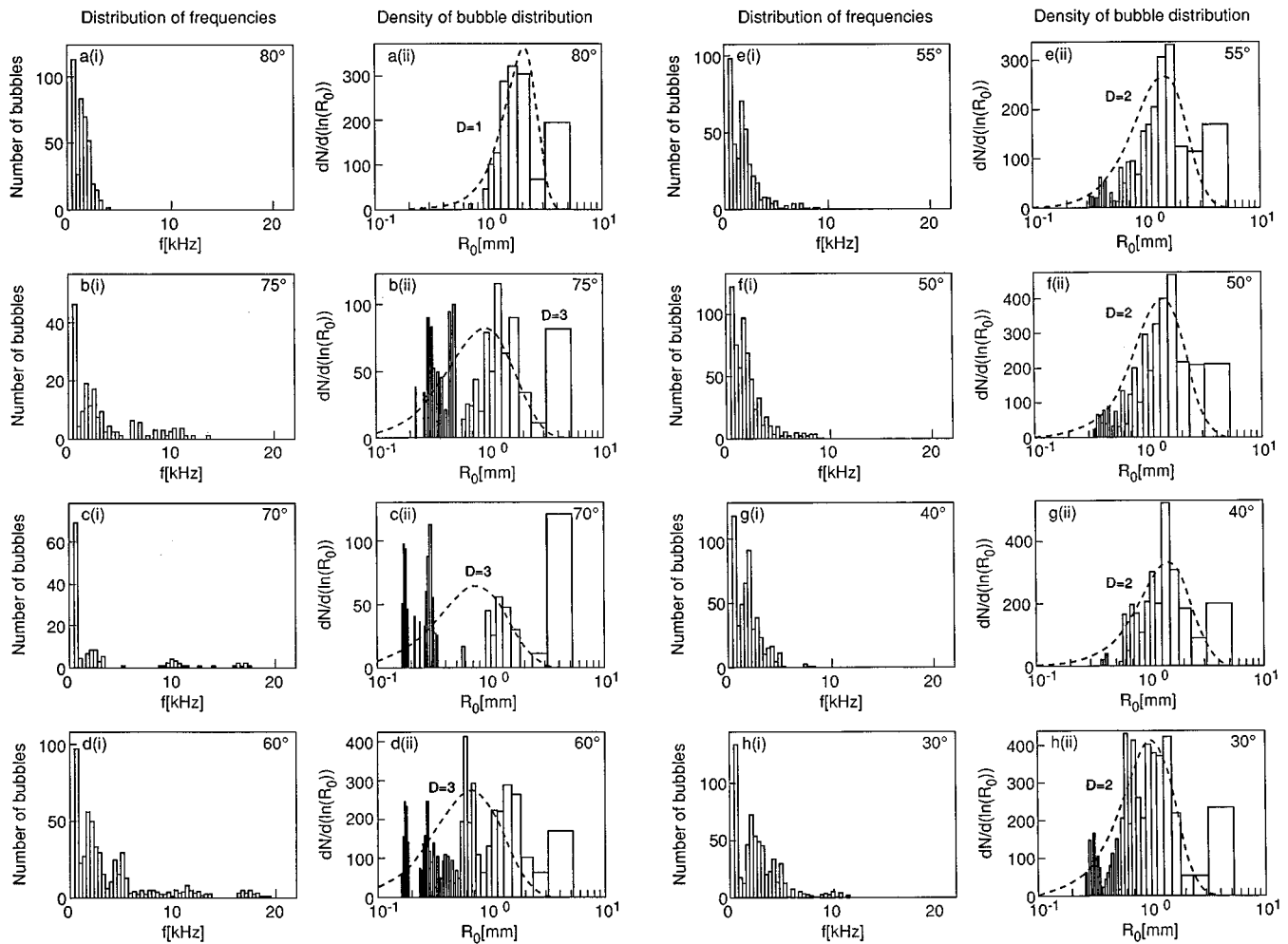
FIG. 13. Histograms of (i) number of bubbles N against bubble natural frequencies f; and (ii) $dN/d[\ln(R_0)]$ as a function of bubble radius R_0. R_0 is normalized to 1 mm. Part (ii) shows the best fit theoretical curves, with the value of D shown (the best-fit value of m is ∞ throughout). Each data set is taken over a period of 5 s. Jet flow rate 2.5 l/min. Surface-to-nozzle angle: (a) 80°; (b) 75°; (c) 70°; (d) 60°; (e) 55°; (f) 50°; (g) 40°; (h) 30°.

this surface is planar and "infinite," and its disturbance causes closure and detachment, and therefore the entrainment of some daughter bubbles. While subsequent break-ups of these bubbles would more closely fit the model, how accurately the free-surface event is described by the theory depends on details of the closure and detachment processes. However, during the period in which these "subsequent break-ups" occur, coalescence might also become an issue: A double peak in the population distribution might, for example, be observed if a preferential bubble size is first formed, and, later, coalesces. In addition to these fluid dynamic issues, contributions from collective oscillations in the waterfall do not reflect bubble entrainment in the same way as single-bubble emissions, but are interpreted as such by the measurement system.

There are other factors inherent in bubble entrainment processes which might more readily be discussed in the light of the assumptions of the theory. Figure 16 shows the fragmentation of large bubbles following injection. The lower bubble has the "hourglass" form characteristic of a shape oscillation dominated by a second-order ($n=2$) axisymmetric spherical harmonic perturbation, an extreme version of which would divide it into two daughters of roughly equal

size (indeed the upper bubble was generated in this way).[40] Such low order shape oscillations may be modeled by the insertion of small numbers of planes at specific sites determined by the mode value, n, and not randomly as the theory[30] assumes. They will generate a number of daughters of similar size, but few bubbles which are either very small or of a size comparable with the mother bubble. As a result one would expect the size distributions obtained experimentally when this occurs to show smaller standard deviations than are predicted by the theory. The assumption of simultaneous insertion will be true for all planes related to minima in a given mode. However fragmentation may occur through a series of sequential shape oscillations, as indicated by the preliminary optical study. Figure 7 shows a "mother" bubble undergoing fragmentation into four bubbles through repeated division into halves. The mother is bisected by a jet, the position of which is determined by a second order ($n=2$) oscillation, and the same fate befalls the resulting two daughters. The description entails the insertion of a single plane associated with the $n=2$ oscillation on three occasions (once in the original bubble, and then once in each of its two daughters). Figure 6 shows a bubble being fragmented by a third-order ($n=3$) shape oscillation, corresponding to the
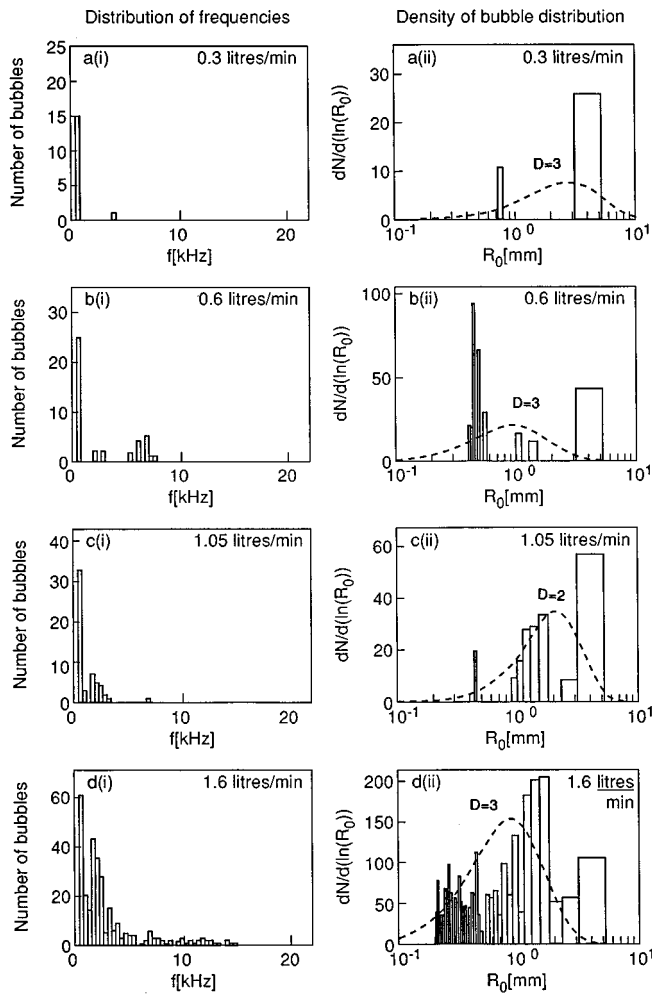
FIG. 14. Histograms of (i) number of bubbles N against bubble natural frequencies f; and (ii) $dN/d[\ln(R_0)]$ as a function of bubble radius R_0. R_0 is normalized to 1 mm. Part (ii) shows the best fit theoretical curves, with the value of D shown (the best-fit value of m is ∞ throughout). Each data set is taken over a period of 4 s. Surface-to-nozzle angle is 55°. Jet flow rate (a) 0.30; (b) 0.60; (c) 1.05; (d) 1.60 l/min.

FIG. 15. Histograms of (i) number of bubbles N against bubble natural frequencies f; and (ii) $dN/d[\ln(R_0)]$ as a function of bubble radius R_0. R_0 is normalized to 1 mm. Part (ii) shows the best fit theoretical curves, with the value of D shown (the best-fit value of m is ∞ throughout). Each data set is taken over a period of 4 s. Surface-to-nozzle angle is 70°. Jet flow rate (a) 0.50; (b) 0.90; (c) 1.05; (d) 3.20 l/min.
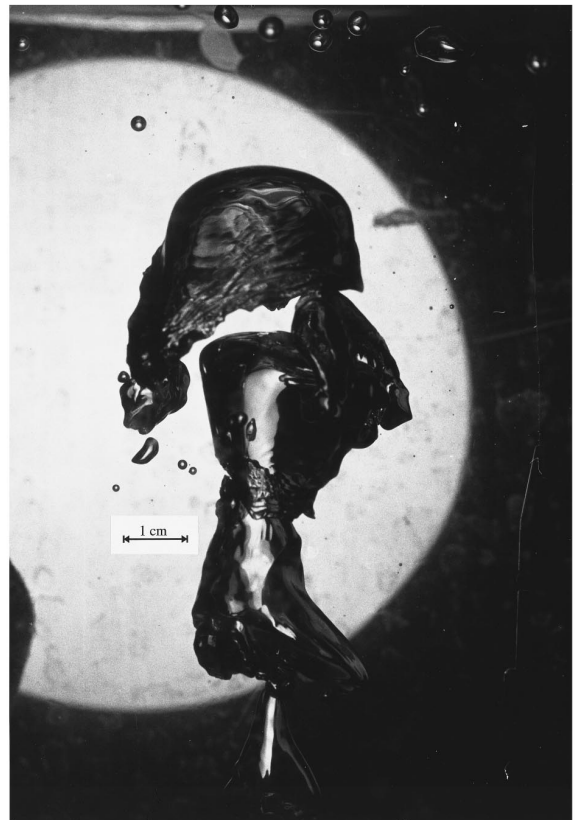
FIG. 16. Photograph of the bubble population produced following injection through a cm radius nozzle.

simultaneous insertion of the two parallel planes associated with the $n=3$ mode, to produce three daughter bubbles.

However Fig. 16 also shows another method of producing daughter bubbles: The small bubbles in the picture were "pinched off" from the peaks of capillary waves visible at the narrowest region of the lower bubble, and over much of the upper bubble. Such capillary wave action can leave the mother relatively intact,[41] equivalent to the simultaneous insertion of planes at positions close to the bubble wall; or may disintegrate the mother entirely.[42]

In a complicated entrainment event a great number of processes may occur, involving (as seen in Fig. 16) both shape oscillations (where plane insertion is biased towards the bubble center) and capillary waves (where the bias is toward the walls). Being based upon a random positioning of planes, it is clear that the theory of Longuet Higgins[30] takes account of neither shape oscillations nor capillary waves on any individual bubble. However it is not clear to what extent the superposition of many shape and surface oscillations oc-
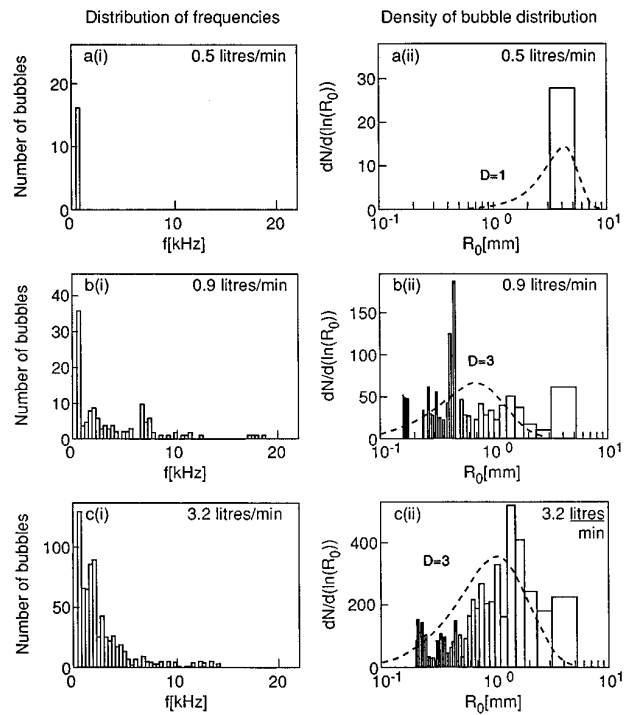
curring in a population may be modeled by a random positioning of planes.

VI. CONCLUSIONS

Data are obtained on the number and size of bubbles produced by bubble entrainment and comminution, both optically (for the comminution of air disk) and acoustically (using an automated signal recognition system for measurements under both waterfalls and plunging liquid jets). Comparison is made with a theory which is based on the breakup of a cubical air pocket. Assumptions regarding the simultaneous insertions of planes at random positions through a single gas body do not take account of the specific ways in which a self-contained air pocket may fragment. Entrainment may often be a population event. It may be the simplicity of the model which makes it versatile as a diagnostic tool for the dimension of bubble breakup under different conditions.

ACKNOWLEDGMENTS

APPENDIX: GABOR EXPANSIONS

Computing the Gabor expansion of a signal is one form of time-frequency analysis. The signal, say $x(t)$, is represented as a sum of scaled time and frequency shifted versions of a prototype signal, $g(t)$, specifically:

$$x(t) = \sum_{n=-\infty}^{\infty} \sum_{k=-\infty}^{\infty} C_{n,k} g(t-n\Delta t)e^{2\pi ik\Delta ft}$$
$$= \sum_{n=-\infty}^{\infty} \sum_{k=-\infty}^{\infty} C_{n,k} g_{n,k}(t), \quad \text{(A1)}$$

where $g_{n,k}(t) = g(t-n\Delta t)e^{2\pi ik\Delta f}$, $C_{n,k}$ are the coefficients of the expansion, and Δt and Δf are the intervals in the time and frequency domains respectively. It should be noted that the representation (A1) maps the continuous time function $x(t)$ to the doubly infinite discrete set $C_{n,k}$. The existence of the representation (A1) is by no means assured. For a suitable function $g(t)$, the sampling grid has to be sufficiently fine,[43] specifically $\Delta t\Delta f \leq 1$.

Representation (A1) allows one to consider $x(t)$ as being made up of a sum of functions of the form of $g_{n,k}(t)$. Many choices of the prototype functions can be made. Gabor[44] considered a Gaussian function of the basic form e^{-t^2}. This choice is problematic since the computation of the expansion coefficients is difficult. Friedlander and co-workers[36,37] present a decomposition based on single sided exponentials, i.e., $g(t)=e^{-\lambda t}$ for $t>0$. The decaying exponential form closely mimics the sound of a decaying bubble and it is this form of Gabor transform which is employed in this paper. By matching the functions, $g_{n,k}(t)$, to the expected data set, the signal representation is efficient and is robust to the adverse affects of noise.

While Eq. (A1) is a representational form, it fails to give information about how to compute the coefficients $C_{n,k}$. This computation is made considerably more simple if the function $g(t)$ and the time-frequency grid are chosen so that $g_{n,k}(t)$ form an orthogonal basis, such that

$$\int g_{n,k}(t)g_{m,1}(t)^* = 0 \quad \text{unless} \ n=m \ \text{and} \ k=1, \quad \text{(A2)}$$

and

$$\int g_{n,k}(t)g_{m,1}(t)^* = \xi \quad \text{for} \ n=k \ \text{and} \ k=1. \quad \text{(A3)}$$

Combining this with Eq. (A1) leads directly to

$$C_{n,k} = \frac{1}{\xi} \int x(t)g_{n,k}(t)^* \ dt. \quad \text{(A4)}$$

It can be shown[43] that if the basis is to be orthogonal then the grid must be such that $\Delta t\Delta f = 1$. However choosing an orthogonal basis is incompatible with the desire for good time and frequency localization of the basis functions.[43]

In cases where $g(t)$ does not generate an orthogonal basis, but is reasonably well behaved, it is possible to define a biorthogonal function,[45] $\gamma(t)$, such that

$$\int g_{n,k}(t)\gamma_{m,1}(t) = 0 \quad \text{unless} \ n=m \ \text{and} \ k=1, \quad \text{(A5)}$$

and

$$\int g_{n,k}(t)\gamma_{m,1}(t) = \xi \quad \text{for} \ n=k \ \text{and} \ k=1, \quad \text{(A6)}$$

where $\gamma_{n,k}(t) = \gamma(t-n\Delta t)e^{2\pi ik\Delta f}$ and hence

$$C_{n,k} = \frac{1}{\xi} \int x(t)\gamma_{n,k}(t)dt. \quad \text{(A7)}$$

The biorthogonal function for the one-sided exponential has a relatively simple analytic form and consequently the Gabor coefficients based on that expansion are conceptually simple to compute. Further, Friedlander and Porat[37] present a highly efficient algorithm, requiring only 2 FFTs.

[1] M. Minnaert, ''On musical air-bubbles and sounds of running water,'' Philos. Mag. **16**, 235–248 (1933).

[2] C. Devin, ''Survey of thermal, radiation and viscous damping of pulsating air bubbles in water,'' J. Acoust. Soc. Am. **31**, 1654–1667 (1959).

[3] M. Strasberg, ''The pulsation frequency of nonspherical bubbles,'' J. Acoust. Soc. Am. **25**, 536–537 (1953).

[4] M. Strasberg, ''Gas bubbles as sources of sound in water,'' J. Acoust. Soc. Am. **28**, 20–26 (1956).

[5] T. G. Leighton and A. J. Walton, ''An experimental study of the sound emitted from gas bubbles in a liquid,'' Eur. J. Phys. **8**, 98–104 (1987).

[6] M. Nicholas, R. A. Roy, L. A. Crum, H. Oguz, and A. Prosperetti, ''Sound emissions by a laboratory bubble cloud,'' J. Acoust. Soc. Am. **94**, 3171–3182 (1994).

[7] A. R. Kolaini, R. A. Roy, and L. A. Crum, ''An investigation of the acoustic emissions from a bubble plume,'' J. Acoust. Soc. Am. **89**, 2452–2455 (1991).

[8] A. R. Kolaini, R. A. Roy, L. A. Crum, and M. Yi, ''Low-frequency underwater sound generation by impacting transient cylindrical water jets,'' J. Acoust. Soc. Am. **94**, 2809–2820 (1993).

[9] A. R. Kolaini, R. A. Roy, and D. L. Gardner, ''Low-frequency acoustic emissions in fresh and salt-water,'' J. Acoust. Soc. Am. **96**, 1766–1772 (1994).

[10] H. N. Oguz, A. Prosperetti, and A. R. Kolaini, ''Air entrapment by a

falling water mass,'' J. Fluid Mech. **294**, 181–207 (1995).

[11] D. Kusabiraki, H. Niki, K. Yamagiwa, and A. Ohkawa, ''Gas entrainment rate and flow pattern of vertical plunging liquid jets,'' Can. J. Chem. Eng. **68**, 893–903 (1990).

[12] D. Kusabiraki, M. Murota, S. Ohno, K. Yamagiwa, M. Yasuda, and A. Ohkawa, ''Gas entrainment rate and flow pattern in a plunging liquid jet aeration system using inclined nozzles,'' J. Chem. Eng. Jpn. **23**, 704–710 (1990).

[13] P. A. Hwang, Y. K. Yu, and J. Wu, ''Temperature effects on generation and entrainment of bubbles induced by a water jet,'' J. Phys. Oceanogr. **21**, 1602–1605 (1991).

[14] F. Bonetto and R. T. Lahey, ''An experimental study on air carryunder due to a plunging liquid jet,'' Int. J. Multiphase Flow **19**, 281–294 (1993).

[15] A. K. Bin, ''Gas entrainment by plunging liquid jets,'' Chem. Eng. Sci. **48**, 3585–3630 (1993).

[16] A. Prosperetti and H. N. Oguz, ''Air entrainment upon liquid impact,'' Philos. Trans. R. Soc. London **355**, 491–506 (1997).

[17] H. C. Pumphrey and A. J. Walton, ''Experimental study of the sound emitted by water drops impacting on a water surface,'' Eur. J. Phys. **9**, 225–231 (1988).

[18] H. C. Pumphrey, L. A. Crum, and L. Bjørnø, ''Underwater sound produced by individual drop impacts and rainfall,'' J. Acoust. Soc. Am. **85**, 1518–1526 (1989).

[19] H. C. Pumphrey and P. A. Elmore, ''The entrainment of bubbles by drop impacts,'' J. Fluid Mech. **220**, 539–567 (1990).

[20] H. Medwin, A. Kurgan, and J. A. Nystuen, ''Impact and bubble sound from raindrops at normal and oblique incidence,'' J. Acoust. Soc. Am. **88**, 413–418 (1990).

[21] H. Medwin and M. W. Beaky, ''Bubble sources of the Knudsen sea noise spectra,'' J. Acoust. Soc. Am. **86**, 1124–1130 (1989).

[22] G. E. Updegraff and V. C. Anderson, ''Bubble noise and wavelet spills recorded 1 m below the ocean surface,'' J. Acoust. Soc. Am. **89**, 2264–2279 (1991).

[23] M. S. Longuet-Higgins, ''An analytical model of sound production by raindrops,'' J. Fluid Mech. **214**, 395–410 (1990).

[24] H. N. Oguz and A. Prosperetti, ''Bubble entrainment by the impact of drops on liquid surfaces,'' J. Fluid Mech. **219**, 143–179 (1990).

[25] J. A. Nystuen, ''Rainfall measurements using underwater ambient noise,'' J. Acoust. Soc. Am. **79**, 972–982 (1986).

[26] J. A. Nystuen and D. M. Farmer, ''The influence of wind on the underwater sound generated by light rain,'' J. Acoust. Soc. Am. **82**, 270–274 (1987).

[27] H. N. Oguz and A. Prosperetti, ''Numerical calculations of the underwater noise of rain,'' J. Fluid Mech. **228**, 417–442 (1991).

[28] F. Laville, G. D. Abbott, and M. J. Miller, ''Underwater sound generation by rainfall,'' J. Acoust. Soc. Am. **89**, 715–721 (1991).

[29] J. A. Nystuen, ''Quantitative rainfall measurement using the underwater sound field,'' in *Proceedings of the Fourth International Meeting on Natural Physical Processes Related to Sea Surface Sound*, edited by T. G. Leighton (University of Southampton, Southampton, 1997), pp. 73–81.

[30] M. S. Longuet-Higgins, ''The crushing of air cavities in a liquid,'' Proc. R. Soc. London **439**, 611–626 (1992).

[31] Y. Toba, ''Drop production by bursting air bubbles on the sea surface III. Study by use of a wind flume,'' Mem. Coll. Sci. Kyoto A **29**, 313–343 (1961).

[32] G. Updegraff, ''In situ investigation of sea surface noise from a depth of 1 meter,'' Ph.D. University of California at San Diego, 1989.

[33] H. Medwin and A. C. Daniel, ''Acoustical measurements of bubble production by spilling breakers,'' J. Acoust. Soc. Am. **88**, 408–412 (1989).

[34] T. G. Leighton, W. L. Ho, and R. Flaxman, ''Sonoluminescence from the unstable collapse of a conical bubble,'' Ultrasonics **35**, 399–405 (1997).

[35] T. G. Leighton, M. F. Schneider, and P. R. White, ''Study of dimensions of bubble fragmentation using optical and acoustic techniques,'' in *Proceedings of the Third International Meeting on Natural Physical Processes Related to Sea Surface Sound*, edited by M. J. Buckingham and J. Potter (World Scientific, Singapore, 1995), pp. 414–428.

[36] B. Friedlander and A. Zeira, ''Oversampled Gabor representation for transient signals,'' IEEE Trans. Signal Process. **43**, 2088–2094 (1995).

[37] B. Friedlander and B. Porat, ''Detection of transient signals by the Gabor representation,'' IEEE Trans. Acoust. Speech Signal Process. **37**, 169–180 (1989).

[38] S. W. Yoon, L. A. Crum, A. Prosperetti, and N. Q. Lu, ''An investigation of the collective oscillations of a bubble cloud,'' J. Acoust. Soc. Am. **89**, 700–706 (1991).

[39] W. Carey and D. G. Browning, ''Low frequency ocean surface noise: Measurement and theory,'' in *Sea Surface Sound*, edited by B. R. Kerman (Kluwer, Boston, 1988), pp. 361–376.

[40] T. G. Leighton, K. J. Fagan, and J. E. Field, ''Acoustic and photographic studies of injected bubbles,'' Eur. J. Phys. **12**, 77–85 (1991).

[41] T. G. Leighton, *The Acoustic Bubble* (Academic, London, 1994), Fig. 4.31.

[42] G. W. Willard, ''Ultrasonically induced cavitation in water: a step-by-step process,'' J. Acoust. Soc. Am. **25**, 669 (1953).

[43] I. Daubechies, ''The wavelet transform: A method for time frequency localisation,'' in *Advanced Spectral Analysis and Array Processing*, Vol. 1, edited by S. Haykin (Prentice-Hall, Englewood Cliffs, NJ, 1991), pp. 366–417.

[44] D. Gabor, ''Theory of communication,'' J. Inst. Electr. Eng. **93**, 429–457 (1946).

[45] M. J. Bastiaans, ''A sampling theorem for the complex spectrogram, and Gabor's expansion of a signal in Gaussian elementary signals,'' Opt. Eng. (Bellingham) **20**, 594–598 (1981).